Available online at www.sciencedirect.com
SCIENCE DIRECT®
International Journal of Heat and Mass Transfer 48 (2005) 1583–1598
International Journal of HEAT and MASS TRANSFER
www.elsevier.com/locate/ijhmt

Predictions of flow and heat transfer in multiple impinging jets with an elliptic-blending second-moment closure

L. Thielen [a,*], K. Hanjalić [a], H. Jonker [a], R. Manceau [b]

[a] Department of Multi-scale Physics, Thermal and Fluids Sciences Section, Delft University of Technology, Lorentzweg 1, 2628 CJ Delft, The Netherlands
[b] Laboratoire d'études aérodynamiques, UMR 6609, University of Poitiers, CNRS/ENSMA, France

Received 19 February 2004; received in revised form 18 August 2004
Available online 15 December 2004

Abstract

We present numerical computations of flow and heat transfer in multiple jets impinging normally on a flat heated surface, obtained with a new second-moment turbulence closure combined with an elliptic blending model of non-viscous wall blocking effect. This model provides the mean velocity and turbulent stress fields in very good agreement with PIV measurements. The exploration of several simpler closures for the passive thermal field, conducted in parallel, confirmed that the major prerequisite for the accurate prediction of the temperature field and heat transfer is to compute accurately the velocity and stress fields. If this is achieved, the conventional anisotropic eddy-diffusivity model can suffice even in complex flows. We demonstrate this in multiple-impinging jets where such a model combination provided the distribution of Nusselt number over the solid plate in good agreement with experiments. Extension of the elliptic blending concept to full second-moment treatment of the heat flux and its truncation to a quasi-linear algebraic model is also briefly discussed.

Keywords: Heat transfer; Impingement; Modelling

1. Introduction

Despite the widespread use of multiple impinging fluid jets for cooling, heating and drying in various areas of engineering, there are still no reliable and sufficiently general correlations that can serve for optimal design of jet configurations for specific applications. The main goal is usually to achieve intensive and uniform heat and mass transfer over the target surfaces, though in some applications, such as electronics cooling, the jets could be focused on specific discrete objects. The optimum performance per unit mass and energy input depends on a number of parameters: nozzles shape and their distance from the target wall, jet spacing and arrangement, the initial flow field and turbulence intensity in the jet, the surrounding near field boundary conditions. In comparison with a single jet, major uncertainties in multiple jets come from possible interaction between jets prior to impingement, but even more from collision of wall jets created on the target surface after the impingement. Depending on the jets configuration,

* Corresponding author. Present address: TNO-TPD Stieltjesweg 1, 2628 CK Delft, The Netherlands. Tel.: +31 15 2692118; fax: +31 15 2692111.
E-mail address: thielen@tpd.tno.nl (L. Thielen).

0017-9310/$ - see front matter © 2004 Elsevier Ltd. All rights reserved.
doi:10.1016/j.ijheatmasstransfer.2004.10.025

Nomenclature

D	nozzle diameter [m]
f	elliptic function [1/s]
H	distance between nozzle plate and impingement plate [m]
k	turbulent kinetic energy [m^2/s^2]
Nu	Nusselt number [–]
q''	total heat flux [W/m^2]
S	distance between nozzles (pitch) [m]
T	temperature [K]
U_i (U, V, W)	Reynolds averaged mean velocity component [m/s]
u_i (u, v, w)	velocity fluctuation [m/s]
$\overline{v^2}$	"wall-normal" velocity scale [m^2/s^2]
x_i	Cartesian space coordinate [m]
x, y	spanwise distance [m]
z	distance from the wall [m]

Greek symbols

α	elliptic parameter [–]
ε	turbulent dissipation [m^2/s^3]
ν	kinematic viscosity [m^2/s]
ν_t	turbulent viscosity [m^2/s]
δ_{ij}	Kronecker delta function [–]
λ	thermal conductivity [W/(mK)]
σ_T	turbulent Prandtl number [–]

Subscripts

b	bulk
w	wall
ref	reference

complex three-dimensional flow patterns may develop, with ejection fountains, recirculation and embedded vortices in the space between the jets, as well as a cross-flow of fluid towards the escape openings. Recent experimental investigations [1,2] provided new evidence of these phenomena and showed that, in some cases, some jets never reach the target plate because of a strong cross-flow from neighbouring jets, thus diminishing the anticipated overall efficiency of the heat transfer. The complex flow pattern will leave a thermal imprint on the target surface with possible large non-uniformities in the heat transfer.

Computational fluid dynamics (CFD) appears as the first choice to serve as a tool for optimising the multiple-jet arrangements for a specific purpose, provided it can be trusted. However, despite years of development, CFD for turbulent flows and heat transfer is still burdened with uncertainties, the major one being in turbulence models for closing the Reynolds averaged momentum and energy equations. Large-eddy simulations may look as a potential alternative, but for high Reynolds numbers wall-bounded flows they require an extremely fine numerical grid to resolve the dominant small-scale structure in the near-wall regions. This in turn puts formidable demands on computer resources, making LES still unusable as a design and optimisation tool.

Heat transfer in single impinging jets has long served as a notorious example of failures of many types of turbulence models, but also as an incentive for their improvement. Success has been claimed by several recent models, primarily those involving elliptic relaxation eddy-viscosity [3,4], non-linear eddy-viscosity [5], and second-moment closures [6,7]. However, computational studies of multiple impinging jets are scarce in the literature and are outweighed by experimental ones. In our earlier publication [8] we reported that the application of the standard k–ε eddy-viscosity model with wall functions returned very erroneous predictions of heat transfer for both of the two jet arrangements (square and circular) considered. Interestingly, Durbin's [10] k–$\overline{v^2}$–f elliptic relaxation model (with integration up to the wall), which was found to work well in single impinging jets and other two-dimensional and axisymmetric flows, was only partially more successful, but still far from satisfactory when applied to three-dimensional multiple-jets. This finding urges for more advanced models, possibly at second-moment level, which should capture the proper dynamics of all stress and heat flux components and their anisotropies. However, because of full three-dimensionality, the absence of symmetry and homogeneity, as well as inapplicability of wall-function and the consequent need to integrate equations up to the wall, solutions of multiple impinging jets can be computationally demanding, especially if more advanced models are employed. In search for a model that would be based on sound physical rationale and yet sufficiently robust to appeal to industry, we have developed a new second-moment closure that meets reasonably well the above requirements. We note, however, that second-moment closures require judicious implementation of the model and adequate modifications of the numerical code to suit the rather different type of mean transport equations when coupled with second-moment models. Such algorithms have been developed and reported, requiring only marginally larger computing time (30–50%) and a small extra effort as compared with conventional low-Re-number k–ε or similar models [11,12].

We report here on a computational study of multiple-impinging jet flows and heat transfer with a second-moment turbulence closure with novel near-wall modifications. Major novelty is the introduction of a topology-free elliptic blending function akin to the elliptic relaxation model of Durbin [13], which has been derived to satisfy the wall constraints and budgets of the model equations. The model proved to be very robust and relatively insensitive to grid density and nonuniformity, thus permitting the use of moderately clustered grids. We show first that the computed velocity and stress field agree very well with the PIV measurements of Geers et al. [1], thus satisfying the main prerequisite for successful prediction of heat transfer. The hydrodynamic model can be extended to treat the thermal field also at the second-moment level. However, because the considered thermal field is passive, in order to diminish unnecessary model complexities we explored several levels of truncation of the transport equations for the turbulent heat flux. As shown below, with adequate velocity and stress field, it is possible to get a reasonable thermal field and heat transfer even with a relatively simple anisotropic eddy diffusivity model ("generalized gradient diffusion hypothesis") for the thermal flux. All results are compared with experiments of Geers et al. [1,2], as well as with two eddy-viscosity models: the standard k–ε with wall functions, and k–$\overline{v^2}$–f model of Durbin [10]. Two nozzle arrangements have been considered, a square and a circular one [8], but results will be shown primarily for the square set-up, which displays some peculiarities and thus poses a greater challenge for computational predictions.

2. Elliptic-blending second-moment closure

2.1. Model of the turbulent stress

The model transport equations for the turbulent stress tensor and the energy dissipation rate, which constitute a second-moment closure, can be written in a general form:

$$\frac{\mathrm{D}\overline{u_iu_j}}{\mathrm{D}t} = P_{ij} + \Phi^*_{ij} - \varepsilon_{ij} + \frac{\partial}{\partial x_k}\left[(\nu\delta_{kl} + C_s\overline{u_ku_l}\tau)\frac{\partial\overline{u_iu_j}}{\partial x_l}\right] \tag{1}$$

$$\frac{\mathrm{D}\varepsilon}{\mathrm{D}t} = \frac{C'_{\varepsilon1}P - C_{\varepsilon2}\varepsilon}{\tau} + \frac{\partial}{\partial x_k}\left[(\nu\delta_{kl} + C_\varepsilon\overline{u_ku_l}\tau)\frac{\partial\varepsilon}{\partial x_l}\right] \tag{2}$$

where P_{ij} and ε_{ij} denote respectively the stress production and their molecular dissipation rate, with $P = 1/2P_{kk}$ and $\varepsilon = 1/2\varepsilon_{ii}$, and Φ^*_{ij} is the velocity–pressure-gradient correlation, known as pressure scrambling term. The latter has long posed the major challenge to second-moment closures, especially for wall-bounded flows because of wall blocking and pressure-reflection effects that cause severe modification of the pressure-scrambling process, primarily towards diminishing its isotropizing effects. Various modifications to account for non-viscous wall effects have shown only partial success: e.g. the early model of Gibson and Launder [14] makes use of wall distance, which is inconvenient in complex flows, and does not work well in stagnation regions, whereas more recent distance-free model of Speziale et al. [15] provides insufficient anisotropization close to a wall. Durbin's [13] elliptic relaxation second-moment closure provides a more general rationale, but requires solution of elliptic differential equations for each component of the tensor function f_{ij} to adjust each stress component to meet the wall budget.

The elliptic blending concept (EBM) of Manceau and Hanjalic [16] follows a different rationale. Here the general elliptic relaxation concept of Durbin is adopted for modeling the inviscid wall blockage effect, but it is used in a different context, i.e. to blend the "homogeneous" (away-from-the-wall) and the near-wall models of Φ^*_{ij}

$$\Phi^*_{ij} = (1-\alpha^2)\Phi^w_{ij} + \alpha^2\Phi^h_{ij} \tag{3}$$

where α is an elliptic blending parameter, obtained by solving an elliptic differential equation

$$\alpha - L^2\nabla^2\alpha = 1 \tag{4}$$

For the "homogeneous" part of the pressure scrambling term, Φ^h_{ij}, any existing "pressure-strain" model can be used. We adopted the model of Speziale et al. [15], which was tuned to return well the stress anisotropy in homogeneous shear flows, as well as in some inhomogeneous flows, though not in the region too close to the wall

$$\begin{aligned}\Phi^h_{ij} = &-\left(C_1 + C_2\frac{P}{\varepsilon}\right)\varepsilon a_{ij} + C_3kS_{ij} \\ &+ C_4k\left(a_{ik}S_{jk} + a_{jk}S_{ik} - \frac{2}{3}\delta_{ij}a_{lk}S_{kl}\right) \\ &+ C_5k(a_{ik}\Omega_{jk} + a_{jk}\Omega ik)\end{aligned} \tag{5}$$

$$a_{ij} = \frac{\overline{u_iu_j}}{k} - \frac{2}{3}\delta_{ij}; \quad S_{ij} = \frac{1}{2}\left(\frac{\partial U_i}{\partial x_j} + \frac{\partial U_j}{\partial x_i}\right); \quad \Omega_{ij} = \frac{1}{2}\left(\frac{\partial U_i}{\partial x_j} - \frac{\partial U_j}{\partial x_i}\right) \tag{6}$$

For the near-wall part, Φ^w_{ij}, we derived a model that fully satisfies the exact wall limits and stress budget:

$$\Phi^w_{ij} = -5\frac{\varepsilon}{k}\left(\overline{u_iu_k}n_jn_k + \overline{u_ju_k}n_in_k - \frac{1}{2}\overline{u_ku_l}n_kn_l(n_in_j + \delta_{ij})\right) \tag{7}$$

where the unit wall-normal vector is evaluated from

$$\mathbf{n} = \frac{\nabla\alpha}{\|\nabla\alpha\|} \tag{8}$$

It is noted that α is a scalar parameter in contrast to Durbin's tensor function. We argue that the elliptic relaxation effect is of a kinematic nature and depends only on the wall topology and the turbulence length scale, but is independent of the stress dynamics.

The dissipation rate of the stress tensor is also expressed in terms of the "homogeneous" and near-wall variables, blended via the same elliptic function α

$$\varepsilon_{ij} = (1-\alpha^2)\frac{\overline{u_i u_j}}{k}\varepsilon + \frac{2}{3}\alpha^2\varepsilon\delta_{ij} \tag{9}$$

For the viscous effect very close to the wall we adopt Durbin's approach, which uses the conventional high-Re-number turbulence time and length scales away from a wall, but with imposed Kolmogorov scales as the lower bounds

$$\tau = \max\left(\frac{k}{\varepsilon};\quad C_\tau\left(\frac{\nu}{\varepsilon}\right)^{\frac{1}{2}}\right);$$
$$L = C_L\max\left(\frac{k^{\frac{3}{2}}}{\varepsilon};\quad C_\eta\left(\frac{\nu^3}{\varepsilon}\right)^{\frac{1}{4}}\right) \tag{10}$$

Exact wall boundary conditions are used for all variables $U_i = 0;\ \overline{u_i u_j} = 0;\ \varepsilon = \frac{2\nu k}{y^2};\ \alpha = 0$

require an analogue second-moment approach to closure of the mean energy equation, i.e. modeling and solving the transport equation for the turbulent heat flux θu_i

$$\frac{\mathrm{D}\overline{\theta u_i}}{\mathrm{D}t} = P^T_{\theta i} + P^U_{\theta i} + \Phi^*_{\theta i} - \varepsilon_{\theta i} + D^\nu_{\theta i} + D^t_{\theta i} \tag{13}$$

where $P^T_{\theta i}$ and $P^U_{\theta i}$ denote production by mean temperature and velocity gradients, respectively, $\Phi^*_{\theta i}$ is the pressure scrambling (temperature–pressure-gradient correlation), $\varepsilon_{\theta i}$ is molecular destruction and $D^\nu_{\theta i}$ and $D^t_{\theta i}$ denote molecular and turbulent diffusion respectively. By following the same approach as for the stress field, we can express the pressure scrambling term with the elliptic blending parameter analogue to Eq. (3)

$$\Phi^*_{\theta u_i} = (1-\alpha^2)\Phi^w_{\theta i} + \alpha^2\Phi^h_{\theta i} \tag{14}$$

For $\Phi^h_{\theta i}$ any known model can be used, whereas for $\Phi^w_{\theta i}$ one can derive an expression analogous to (7). Likewise, the dissipation rate $\varepsilon_{\theta i}$ can also be expressed in terms of elliptic blending, but at high Re number flows this term is significant only close to a solid wall, where it can be expressed in standard form as $\varepsilon_{\theta i} = \varepsilon(\overline{\theta u_i}/k)$.

For complex 3D flows the application of a full second-moment model for the turbulent heat flux can be computationally too demanding. A compromising route

C_s	C_ε	$C^0_{\varepsilon 1}$	$C_{\varepsilon 2}$	C_1	C_2	C_4	C_5	C_τ	C_L	C_η
0.21	0.18	1.44	1.83	1.7	0.9	0.625	0.2	6.0	0.161	80.0

and

$$C_3 = 0.8 - 0.65A_2^{1/2} \tag{11}$$

$$C'_{\varepsilon 1} = C^0_{\varepsilon 1}\left(1 + 0.03(1-\alpha^2)\sqrt{\frac{k}{\overline{u_i u_j}n_i n_j}}\right) \tag{12}$$

It should be mentioned that the EBM used here differs slightly from the original model of Manceau and Hanjalic [16]. The differences appear in Eq. (4) where on the right-hand-side we now use "1" instead of $1/(\varepsilon\tau)$, and in Eqs. (3) and (9) where α^2 is used instead of the products $(k\alpha)$ in (3) and $(Ak\alpha)$ in (9) as originally proposed (where A is Lumley's stress "flatness" invariant). A slight readjustment of the model coefficients, tuned in a channel flow, was also made to compensate for the model changes. These modifications were introduced to improve model robustness without deteriorating its performances.

2.2. Model of the turbulent heat flux

A consistent modeling of heat transfer in conjunction with the elliptic blending model for the stress field would is often followed by which a heat flux model is adopted at a lower modeling level, the argument being that good predictions of velocity and stress field can "tolerate" a cruder and simpler heat flux model, especially if the thermal field is passive. We considered several levels of truncation of equation to an algebraic form. By adopting a quasi-linear model of the pressure-scrambling term [17] (which is strictly valid only for Φ^h_θ)

$$\Phi^*_{\theta i} = -C_{\theta 1}\tau(\overline{\theta u_i} - 1.5a_{ij}\overline{\theta u_j}) - C_{\theta 2}P^U_{\theta i} - C'_{\theta 2}P^T_{\theta i} \tag{15}$$

and applying the weak-equilibrium assumption for $\overline{\theta u_i}$, Eq. (15) can be truncated to yield a convenient algebraic model for the heat flux

$$\overline{\theta u_i} = -C_{\theta 1}\tau\left[(1-C'_{\theta 2})\overline{u_i u_j}\frac{\partial T}{\partial x_j} + (1-C_{\theta 2})\overline{\theta u_j}\frac{\partial U_i}{\partial x_j}\right] + 1.5a_{ij}\overline{\theta u_j} \tag{16}$$

This model has been tested successfully in several natural and mixed convection flows (of course with addition of buoyancy term [17]), showing very good performances.

However, one can go a step further and omit all terms except the first one, reducing the expression to

the well-known anisotropic eddy-diffusivity model for heat flux (known also as generalized gradient diffusion hypothesis, GGDH).

$$\overline{\theta u_i} = -C'_\theta \frac{k}{\varepsilon} \overline{u_i u_j} \frac{\partial T}{\partial x_j} \tag{17}$$

This last truncation step from Eqs. (16) and (17) may look unjustified if the full second-moment closure is solved for the stress field, especially because all terms in (16) are available. However, the GGDH model (17) has been widely popular and we explore its performance in the framework of the EBM second-moment closure. The coefficient C'_θ has been chosen from the equilibrium near-wall conditions, where the standard isotropic eddy-diffusivity model $\overline{\theta u_i} = -\nu_t/\sigma_T \partial T/\partial x_i$ suffices, where $\nu_t = C_\mu k^2/\varepsilon$. For $C_\mu = 0.09$, $\sigma_T = 0.85$ and $\overline{u_2^2}/k = 0.35$, this leads to $C'_\theta = \frac{C_\mu k}{\sigma_T \overline{u_2^2}} \approx 0.3$.

3. Flow configuration and numerical details

3.1. Geometry, flow conditions and computational domain

A detailed description of the two multiple-jet configurations, the square and circular one, can be found in Thielen et al. [8] and Thielen [9], and it will suffice to list only the main parameters of the square set-up that is here in focus. The set-up mimics the experimental configurations of Geers et al. [1] and Geers [2], which consists of a plate with nine circular sharp-edged orifices, placed at the end of a settling chamber that was preceded by a square contraction of 2.8:1 area ratio and a set of honeycombs and gauzes. This ensured uniform jets velocity and virtually no inflow turbulence, making it possible to replicate computationally the experimental inflow conditions. The fluid escapes radially through the exit area between the two plates at the edges of the nozzle plates. At these outlet cross-sections we imposed the pressure boundary conditions. The distance between the nozzles (S) and from the nozzle plate to the target impingement plate (H) were both $S/D = H/D = 4$. The Reynolds number for all calculations, based on the diameter of the nozzle (13 mm), jets initial bulk velocity of 23.88 m/s and properties of air, was $Re_D \approx 20000$. The jet arrangement, dimensions and Re number have been selected to be close to some common applications, such as in industrial bakery ovens.

In order to economize with the number of grid cells, we took advantage of the jets set-up geometrical symmetry and adopted only one quarter of the flow as the computational domain, with imposed symmetry conditions on the two inner boundaries. As discussed below, the computations yielded an asymmetric flow pattern (later confirmed by experiments), what prompted additional computations over the whole flow domain, but these reproduced well the findings in the quarter of the solution domain. A sketch of the square set-up, the solution domain and of the planes in which the computational results were compared with experimental data, are shown in Fig. 1.

3.2. Computational method and numerical grid

The computations were performed using the in-house finite-volume CFD code "X-Stream", with non-orthogonal multi-block structured collocated grid arrangement. The convective terms were discretised with the second-order accurate UMIST flux-limiting TVD scheme. Linear and quadratic upwind schemes, LUDS and QUICK are also available in the X-Stream code and were used occasionally for comparison with the TVD scheme. The central differencing was used for all diffusion terms. The second-moment closure was implemented in a predictor-corrector manner via an artificial eddy diffusivity for the shear components of the Reynolds stress tensor (e.g. [12]).

The numerical grid used for the calculations of the square set-up with the EBM and k–$\overline{v^2}$–f models consisted of approximately 430.000 control cells divided in 37 blocks. In the wall-normal direction the blocks were divided in 99 cell layers, clustered towards the wall, Fig. 2. For the k–ε model with wall functions the mesh consisted of about 115000 cells, with uniformly spaced 25 cell layers in the wall-normal direction.

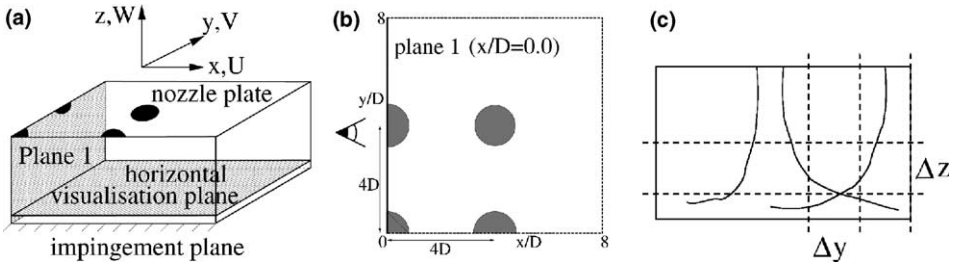

Fig. 1. The computational domain (one quarter of the flow) (a), the position of the planes on which the results are visualized (b) and a sketch of the location of the profiles presented (c). The eye indicates the view direction used to visualize the planes. Dashed lines indicate the lines along which the profiles are plotted.

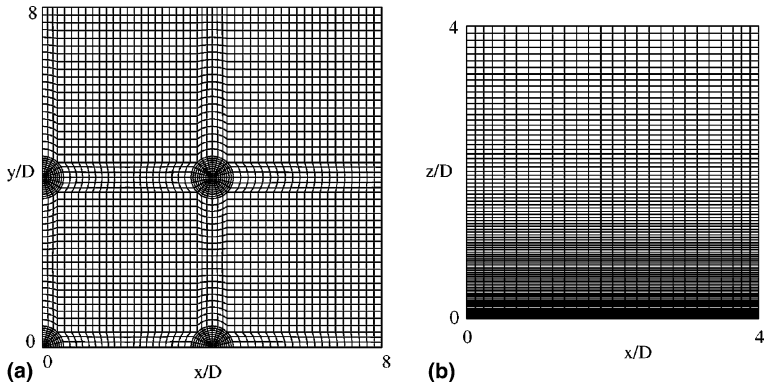

Fig. 2. Distribution of grid cells for the square set-up with indicated nozzles: (a) top-view; (b) side view of grid clustering for the k–$\overline{v^2}$–f and EBM models.

4. Results and discussion

The computations are compared with recent experimental results of Geers et al. [1,2], who provided two-component particle-imaging velocimetry (PIV) data for the flow field and turbulence statistics, and liquid crystal thermography (LCT) measurements for the heat transfer on the impingement plate. The computational results are presented for the quantities for which the experimental data are available. For a general view of the flow field, results on planes in the domain will be shown. The positions of the visualization planes in the domain for the square set-up can be seen in Fig. 1. For a more detailed comparison with experiments, profiles of variables at selected locations will be shown. In the vertical plane (plane 1), two "sets" of profiles are presented. In one set the lines, along which profiles are shown, are parallel to the impingement plane. The profiles are evaluated at $z/D = 3.5$, 2.5, 1.5, 0.5 and 0.1. For the second set the lines are perpendicular to the impingement plane. The locations are $y/D = 0.0$, 0.5, 1.0, 1.5, 2.0, 2.5, 3.0, 3.5 and 4.0. A sketch of the positions of the profiles is given in Fig. 1. We begin first with the presentation and discussion of the velocity and turbulence variables, and then move to heat transfer. The field data are presented in four parallel plots to facilitate the comparison and judgement of model performances: computational results obtained with the standard k–ε model with wall functions, with the k–$\overline{v^2}$–f model and elliptic blending second-moment closure (EBM) and experimental data.

4.1. Flow field

The velocity vectors in plane 1 are shown in Fig. 3. The common feature of the computations with the k–ε + WF and k–$\overline{v^2}$–f model is the pronounced outward shift of the left side jet in strong contrast to the experimental evidence and EBM results. Experiments show only a slight shift of the side jet with an upward fountain caused by the collision of the wall jets roughly in the middle between the two jets (at $y/D \approx 2.2$), separating two asymmetric recirculation regions. Note that the vector plots are the field slices in this plane of the complex vortical structure, a torroidal-type vortex that envelopes the central jet and horse-shoe vortices enveloping the side jets. The velocity field with all features mentioned above is very well captured with the EBM, except that the computed jets seem slightly thicker than the experimental ones. It is noted that the diameter of the experimental jets is slightly smaller than D because of the *vena contracta* effect that characterizes jets emerging from sharp-edged constant-area nozzles, as used in the experimental set-up. The *vena contracta* effect was not accounted for in the computations where a uniform initial jet velocity was assumed over the full diameter. In contrast to experiments and EBM, the k–ε and k–$\overline{v^2}$–f models resulted both in only one central recirculation pattern, with an embedded smaller vortex just beneath the side jet preventing its full impingement on the target plate.

The contour plot of the wall normal velocity, indicating clearly the velocity magnitude, Fig. 4, confirms further the above findings and very close similarity between the experiments and EBM predictions, contrasted with the failure of the k–ε and k–$\overline{v^2}$–f models. An upwash between the jets is also produced by these two eddy viscosity models, but much closer to the disturbed side jets, centred at about $y/D = 3.5$ for the k–ε result and even at $y/D = 4.0$ for the k–$\overline{v^2}$–f model. This is a consequence of the unrealistically large disturbance, predicted by these models, as compared to the experimental data and EBM.

The effect of the outward shift can also be seen in the contour plots of the wall-parallel velocity component, shown in Fig. 5. The wall jet of the right jet extends past $y/D = 2$ in the computations, especially for the k–ε and k–$\overline{v^2}$–f results. The results also show the benefits of the integrating up to the walls, as used by the k–$\overline{v^2}$–f model and EBM, in comparison to the wall function approach

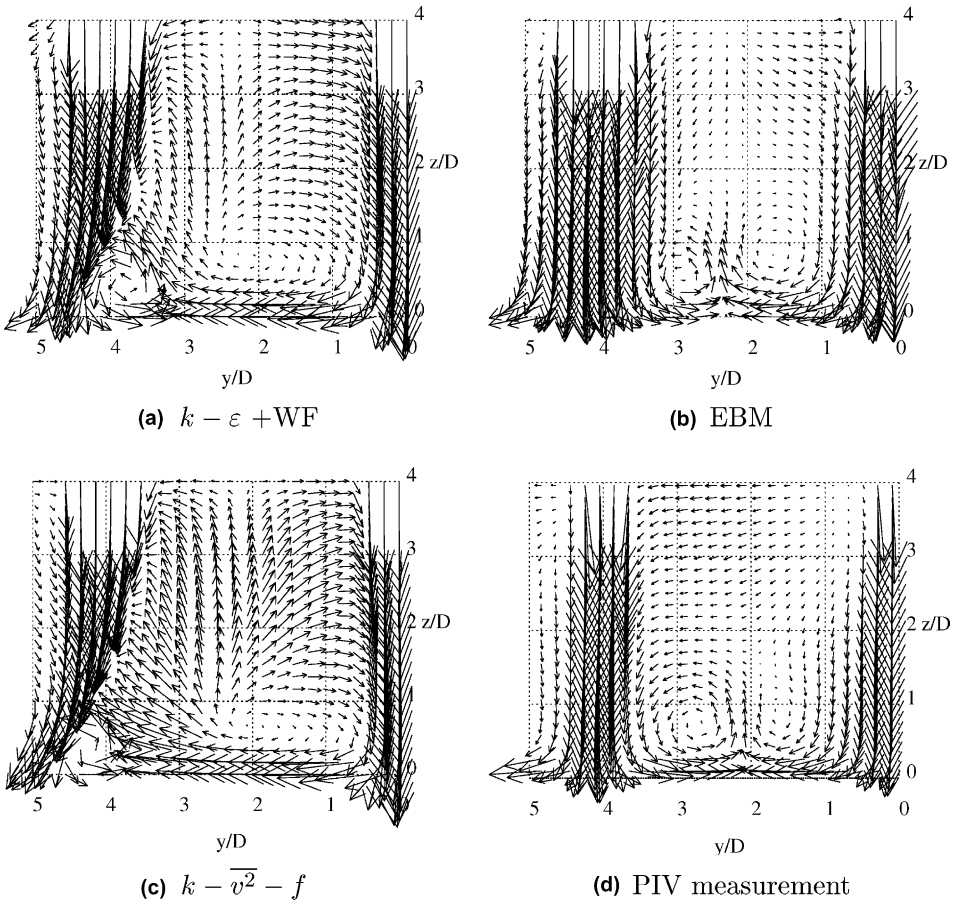

Fig. 3. Square set-up: velocity vectors in plane 1 ($x/D = 0.0$). (for clarity, the vectors are plotted only in selected computational points).

of the k–ε model. Integration up to the wall results in a better resolved wall jet, as can be seen from the isolines near the impingement wall. The EBM result is closest to the experimental data.

The computed components of the Reynolds-stress tensor reflect the general trend of the velocity field. An overview of the quality of predictions with different models is depicted in Fig. 6 showing the contours of the shear stress component $\overline{vw}$. Again the results reveal the shift of the disturbed jet, which is clear from the shear layer at the right edge of the left jet. The contour plots show again that EBM model returns the stress distribution in the planes considered closest to experiments, though the peak intensity is somewhat lower.

4.2. Mean velocity and turbulent stress profiles

We move now to compare profiles of the mean velocity and stress components in several characteristic planes for which the experimental data are available. Fig. 7 (left) shows the wall-normal W and one of the plate-parallel component V of the mean velocity along the horizontal lines in Plane 1 at different heights above the impingement plane (normalised with the jet bulk velocity W_b). The top profiles ($z/D = 3.5$) are located at $0.5D$ below the nozzle exits ($z/D = 4$) and the bottom profiles at $z/D = 0.1$ are just above the impingement plate. The axis of the central jet is located at $y/D = 0.0$, while $y/D = 4.0$ is the location of the centre of the side jet.

The profiles of the wall-normal velocity component W/W_b at the cross-section nearest to the nozzle plane ($z/D = 3.5$) reflect the inflow field with clear identification of the two jets, with uniform velocity in the jet centres (potential core), shear layers at the jet edges and zero velocity in between. At this location the experiments show very thin shear layers, which were difficult to resolve experimentally: hardly any measuring points are visible here. All models considered, produce somewhat thicker shear layers. The difference between the computations and experiments originates most probably in the *vena contracta* effect. This, seemingly important detail, was not accounted for in the computations where uniform inlet profiles are imposed at the inlet boundary.

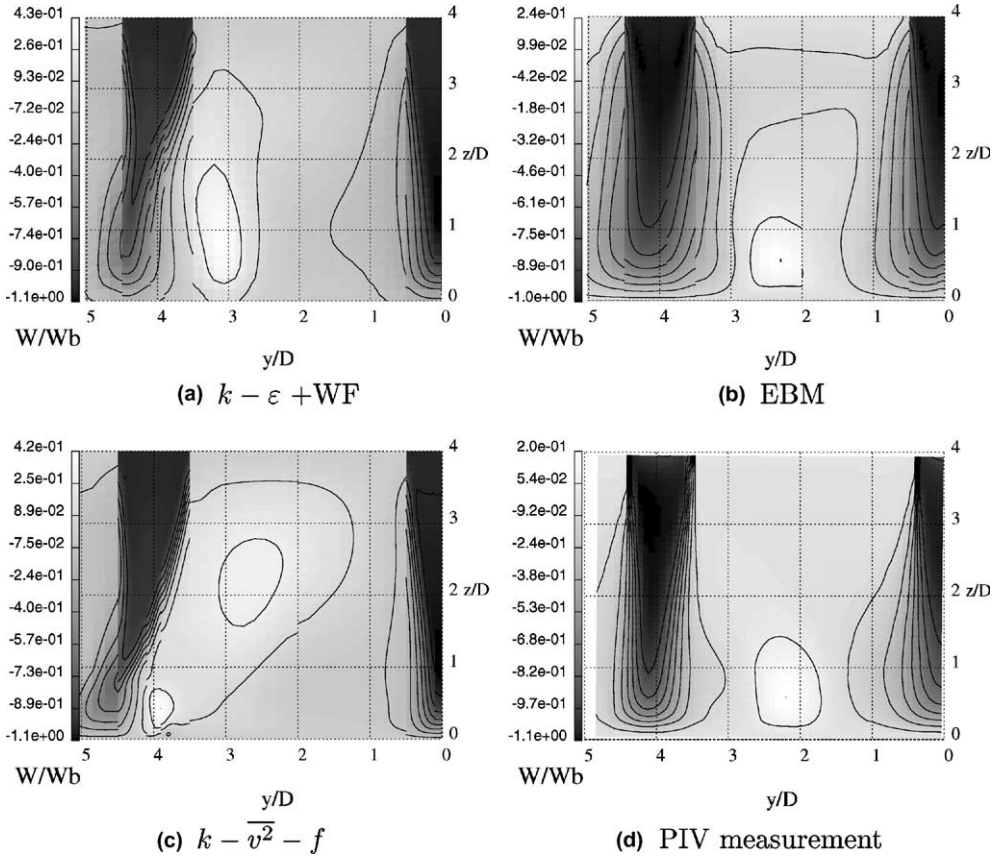

Fig. 4. Square set-up: contours of velocity component normal to the impingement plane, scaled with the jet bulk velocity (W/W_b), in Plane 1 ($x/D = 0.0$).

The profiles in the upper area are symmetric around the mid-spacing between the jets ($y/D = 2.0$) and this symmetry persists in experiments roughly half-way downstream (up to about $z/D \approx 2$). The development, lateral expansion and eventual mutual interaction of the jets are clearly visible. Experiments show that the outward shift of the side jet begins roughly at $z/D = 2$, as indicated by the profile asymmetry with respect to the jets initial mid-distance. The experimental peak velocity in the side jet moves gradually from $y/D = 4.0$ at the inlet to about 4.2 at $z/D = 0.5$ what is not significant, except that this trend becomes stronger when moving still closer to the impingement plate, as already shown in Figs. 3 and 4.

The predictions of the velocity profiles with different models show very different spreading rates. Again the EBM yields profiles closest to experiments although with somewhat larger spreading rate in the upper zone (down to $z/D = 1.5$), probably due to lack of full matching of the inlet conditions. What matters, however, for the problem here considered, is the flow field close to the impingement plate and here the EBM computations show excellent agreement with experiments, reproducing well the velocity profiles not only within the jets, but also in the space between them. The location and intensity of the upwash are well reproduced and so is the corresponding outward shift of the outer jet. The computations with the k–ε model and k–$\overline{v^2}$–f model show both large discrepancies from experimental data, with overestimated jets interaction and consequently a much stronger shift of the side jet.

The wall-parallel velocity (V) profiles show very small values in most of the domain outside the wall jets on the impingement plane, confirming that the motion is primarily in vertical direction. All computations show V profiles close to the experimental ones, with only minor discrepancies. For example, close to the nozzle plate experiments show small positive values of V along the whole cross-section, whereas all computations produce weak negative motion close to the central jet and positive close to the side jet with zero average. In the central region all computations show behaviour similar to the experimental one. It is suspected that because of very small velocity magnitude, the measured data are within

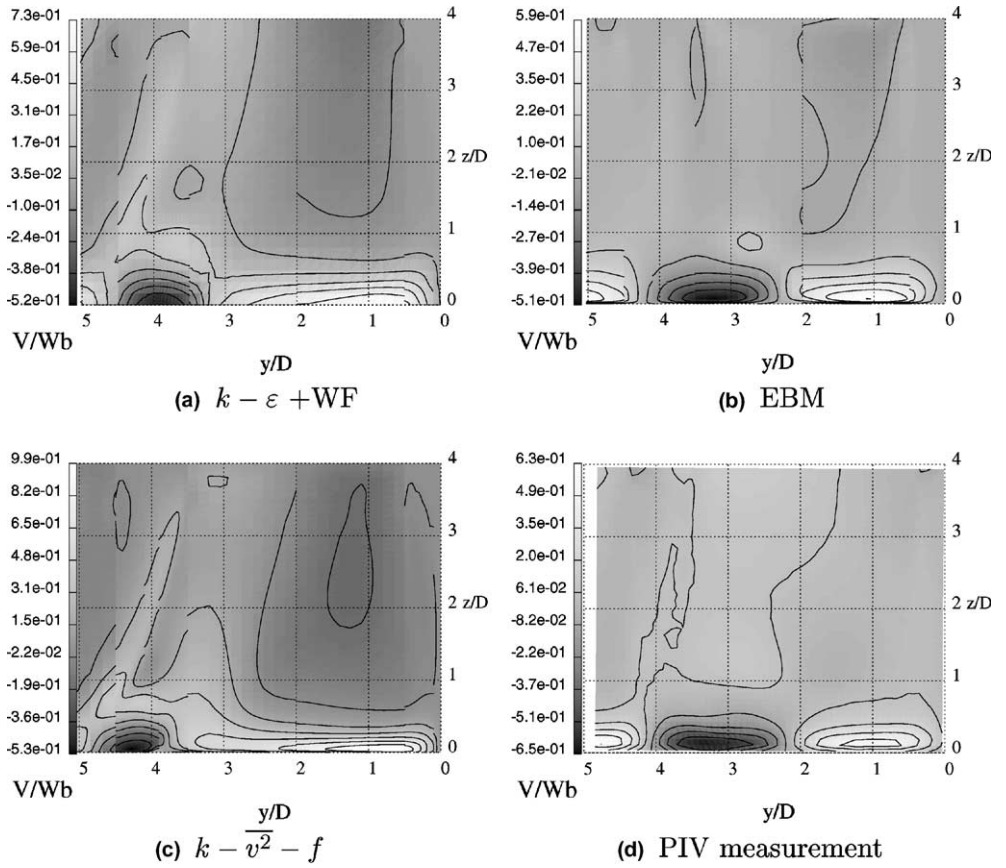

Fig. 5. Velocity component parallel to the impingement plane, scaled with the jet bulk velocity (V/W_b), in Plane 1 ($x/D = 0.0$). The wall jet of the undisturbed jet extends beyond $y/D = 2.0$.

the experimental scatter, and thus not fully reliable, but because of generally very weak horizontal motion, this is not much of relevance. However, in the wall jet region (profiles at $z/D = 0.5$ and $z/D = 0.1$) the predictions with three models give very different outcome. At $z/D = 0.1$ experiments show close to sinusoidal variation, almost symmetric around the position $y/D = 2.2$ where V/W_b changes the sign (from positive to negative when moving from central to side jet) with both the positive and negative peaks around $V/W_b \approx 0.6$. The same behaviour can be seen at $z/D = 0.5$ with much smaller peak values, indicating that this position is roughly at the edge of the wall jet, as can also be seen in Fig. 5. In the contour plot computed with the k–ε model and k–$\overline{v^2}$–f model (Fig. 5a and c) the wall jet of the central jet extends beyond $y/D = 1.0$. These two models give also very erroneous V profiles at both position, $z/D = 0.5$ and $z/D = 0.1$, with the change of sign from positive to negative V/W_b located at $y/D = 3.0$ for the k–ε result and at $y/D = 3.5$ for the k–$\overline{v^2}$–f result. Again the EBM results are much closer to the experiments in every respect, reproducing very similar profile shape, the location of the sign change ($y/D \approx 2.4$) and the peak values of V/W_b.

The profiles of the two components of the turbulent stress, the wall-normal stress $\overline{ww}/W_b^2$ and the shear stress $\overline{vw}/W_b^2$ in Plane 1 are presented in Fig. 7 (right). Here none of the models reproduced results in satisfactory agreement with measurements, though EBM results are somewhat closer. The main deficiency shown by all models is in capturing the peaks of the turbulent stresses, which were underpredicted by all models. Whilst this failure could be anticipated—especially for the normal stress components- with any eddy viscosity model, be it k–ε and k–$\overline{v^2}$–f type, the EBM was expected to provide a reasonable stress field. We suspect that the source of discrepancy could be in the difference in the inflow conditions. In the experiment, the measurements detected sharp peaks of all stress components at the jets edges even very close to the nozzle plane, i.e. at the very early stage of jets development, indicating that the initial stress profiles were not uniform as originally expected and assumed in the computations. These sharp stress

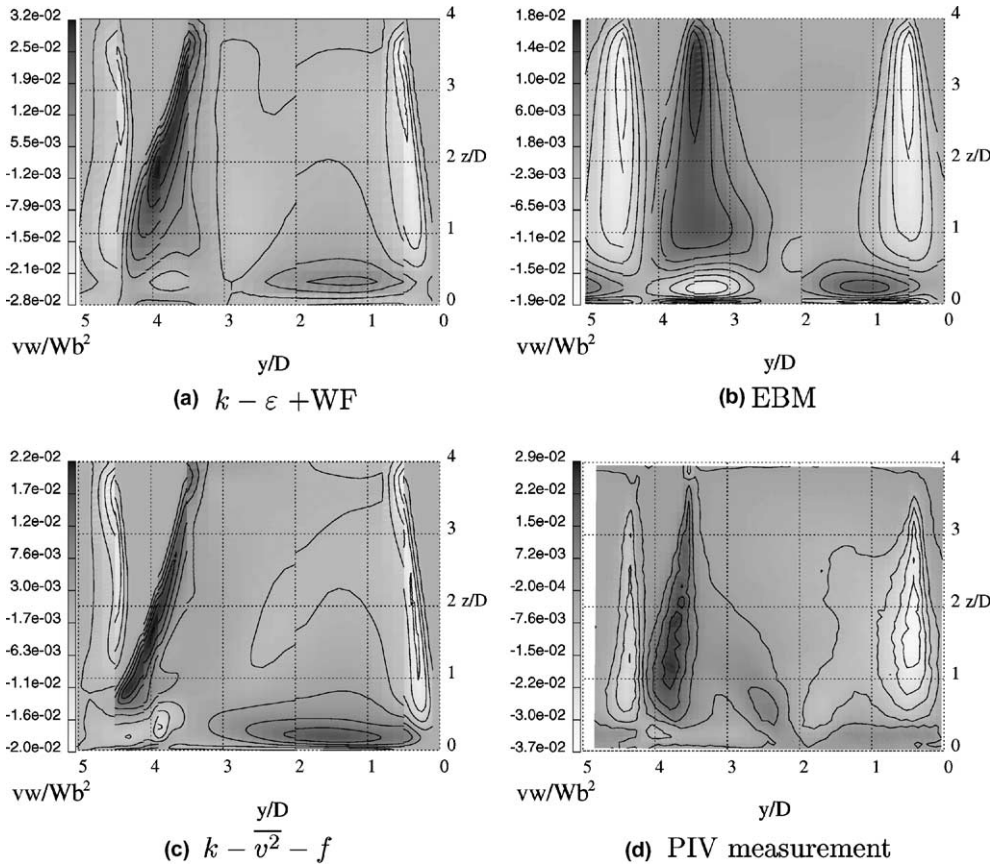

Fig. 6. Shear stress contours in Plane 1, scaled with the jet bulk velocity ($\overline{vw}/W_b^2$).

peaks in the experiments were probably generated by strong velocity gradients originating from the sharp orifice edge and *vena contracta*. Apart from peak values, the general trend is well reproduced, especially of the shear stress, with EBM being marginally better than other two eddy viscosity approaches.

The growth of the shear layers can be depicted from the evolution of the stress profiles and their peak values, when moving from $z/D = 3.5$ to $z/D = 1.5$ At lower positions the damping effect of the impingement wall lowers the stress. Because of the large disturbance of the jet, the computations only show one peak near $y/D = 4.0$ for the results of the k–ε model and k–$\overline{v^2}$–f model. This is caused by the fact that this shear layer extends past $y/D = 4.0$ (see Fig. 6a and c) and as a result "blocks" the shear layer on the other side of the jet, so the second peak is not present. In the EBM result still a second peak can be seen. Because the $\overline{vw}$-component in the experiments is also uniform at the nozzle exit, the computed values are closer to the experimental data. The k–ε and k–$\overline{v^2}$–f models give similar predictions. Again, only one peak can be observed in the computations at $z/D = 0.5$, while the experiments show two peaks. This difference is caused by the larger shift of the jet predicted by the computations. The EBM result does show two peaks, although the gradients of the shear stress are less strong, which results in a smoothing of the peak profiles. In the contour plot of the experimental result (Fig. 6d), a small region with high values can be seen around $y/D = 2.5$. This peak is also apparent from the profile at $z/D = 0.5$. Only the EBM model is able to capture this trend.

Vertical profiles of the velocity components are presented in Fig. 8. Note that $y/D = 0.0$ is the centre of the central jet, while $y/D = 4.0$ is the centre of the side jet. The measured wall-normal velocity shows first a small increase at the jet exit as a consequence of the *vena contracta*, then takes an almost constant value down up to $z/D \approx 2.0$ when it starts gradually to diminish, and then, after $z/D = 0.5$, approaches steeply to zero wall value at the impingement wall. Computations with all models follow this trend, apart from the initial acceleration, which, as discussed above, was not accounted for. The k–ε + WF and k–$\overline{v^2}$–f models predict a delay in

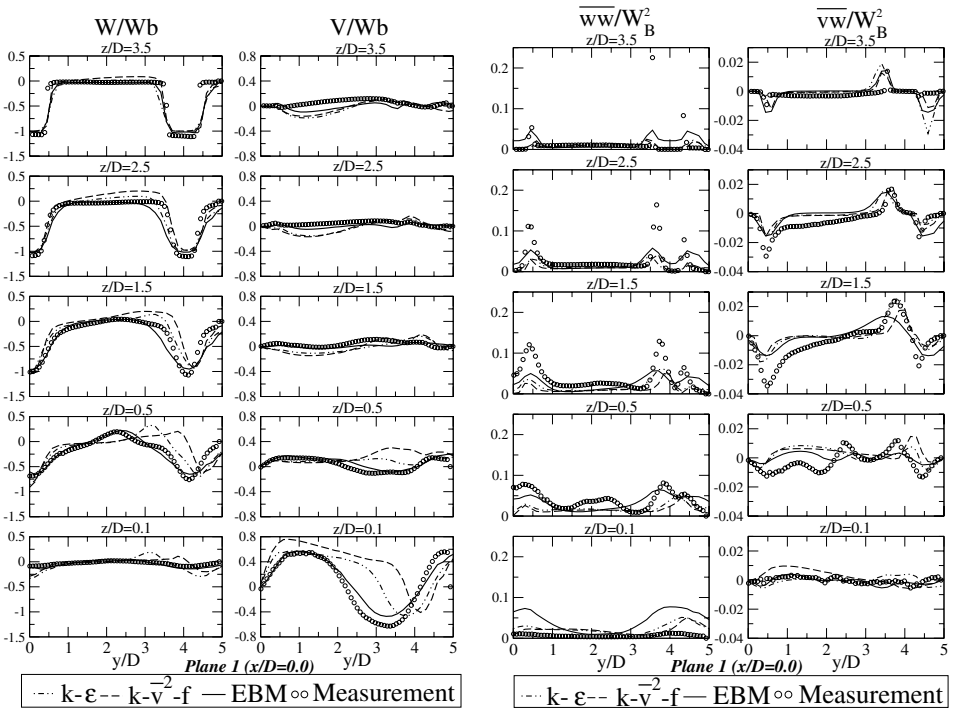

Fig. 7. Velocity components (left) and turbulent stress components (right) along wall-parallel lines in plane 1 at different distance from the impingement wall.

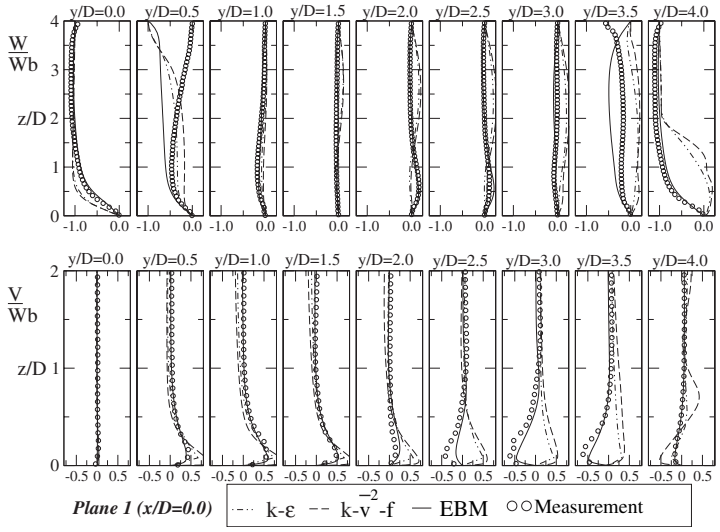

Fig. 8. Profiles of the two velocity components ((above) wall normal and (below) wall-parallel) along vertical lines in Plane 1.

velocity adjustment up to $z/D \approx 0.7$, followed by a much steeper approach to zero value at the wall. In contrast, the EBM provides almost perfect agreement.

At $y/D = 0.5$ and $y/D = 3.5$ the agreement seems bad. However, the difference between the measured and computed results originates from the fact that this line corresponds exactly to the edge of the jet at its exit and that the measuring and computing planes are not fully coincident. The measurements are taken just outside the jet, while the computed profiles are inside the

jet. This results in a value of $W/W_b = 0.0$ for the experiments, while the computed value is $W/W_b = -1.0$ at this location (at $z/D = 4.0$). At $y/D = 4.0$ the difference between the experiments and the computations with the k–ε model and k–$\overline{v^2}$–f model is very large, illustrating the failure of these two models to predict the real interaction between the two jets, whilst the EBM returns excellent predictions. Here the measurements and the EBM show a profile similar to that at $y/D = 0.0$, whereas the k–ε model and k–$\overline{v^2}$–f model start to deviate at $z/D = 2.0$, because of the unrealistic outward shift of the side jet.

The profiles of the wall-parallel velocity component V/W_b (shown only for the lower half of the domain $z/D = 0.0$–2.0 to blow up the near-wall region) display clearly the development of the wall jet, issuing from each jet and then colliding. A typical wall-jet peak in the profile develops along the wall, first increasing and then decreasing, approaching the location of collision of the two opposing wall jets. This behaviour is mirrored in the two wall jets originating from the centre and side jets. Experiments show that the collision in Plane 1 here considered occurs approximately at $y/D = 2.2$, as also seen clearly in the contour plot in Fig. 5. These complex wall-jets interactions, the evolution of the wall-parallel velocity with the change of sign at the collision location, are all very well reproduced by the EBM model, save for a small underprediction of the negative velocity peaks at $y/D = 2.5$–3.5. In contrast, the k–ε and k–$\overline{v^2}$–f results are very erroneous: they fail by far to reproduce the collision location and give a too strong wall jet issuing from the centre jet, with its velocity remaining positive almost up to the centre of the side jet.

We focus now on the results in the horizontal wall-parallel plane, close to the bottom impingement plate and discuss the flow pattern and its relation with the thermal imprint on the wall. As seen below, capturing accurately the velocity and stress close to the wall is the major prerequisite for accurate prediction of wall heat transfer. In Fig. 9 we compare the computed and measured velocity vectors in the plane at $z/D = 0.54$ for which the measurements are available, though only for the mean velocity. The striking impression from all figures is the lack of diagonal symmetry despite the fact that the imposed flow conditions are symmetric with respect to vertical, horizontal and diagonal lines passing through the centre of the central jet. The computational outcome is even more surprising because symmetry conditions have been imposed along the left and lower boundary of the computational domain containing one quarter of the complete set-up. It is noted that in all cases fully convergent solutions have been achieved. Various computational tests, as well as experiments, confirmed that this asymmetry is not an artefact, but a

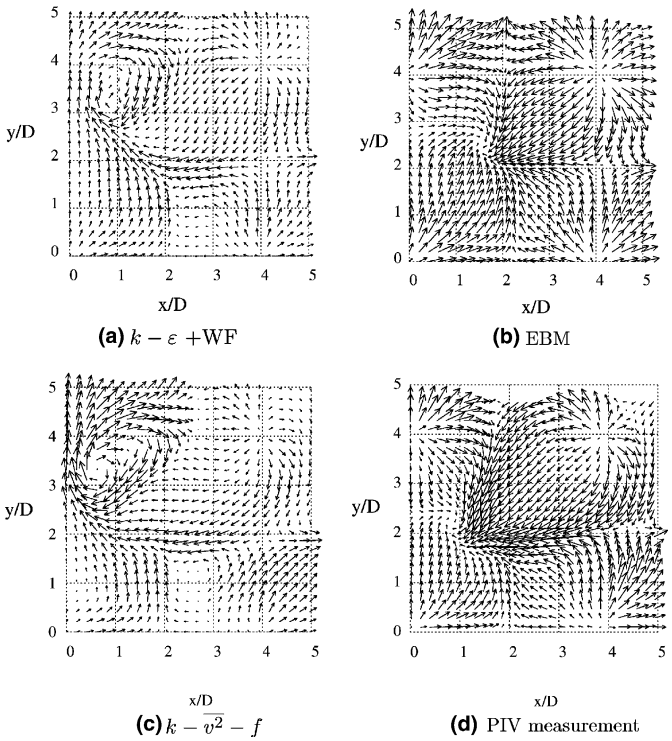

Fig. 9. Velocity vectors in a plane at $z/D = 0.54D$ above the impingement wall (plotted for clarity only in selected grid points).

true feature of the flow with the square jet set-up. The origin of dissymmetry is believed to be in a low-momentum embedded vortex that is displaced from the diagonal either in one or other direction (depending on the initial disturbance and sequence of solution of equations during the solution procedure). Interestingly, this asymmetry was not found in the circular nor in hexagonal set-ups; for more details see Geers et al. [1] and Thielen et al. [8]. The intensity of this vortex in the experiments is relatively small. The computations with the $k-\varepsilon$ and $k-\overline{v^2}-f$ model predict a much stronger vortex-like structure. Also the location is different. The EBM predicts a small vortex structure of the intensity very similar to the experimental one and at almost the same location as in the experiments.

4.3. Heat transfer

We present now some results of heat transfer computations, obtained with the full elliptic blending second-moment closure (EBM) for the velocity and stress fields (Eqs. (1) to (12)) implemented into the Reynolds-averaged momentum equation), and the conventional anisotropic eddy diffusivity model, GGDH, (Eq. (17) for the turbulent heat flux implemented into the mean energy equation). Although the use of this relatively simple eddy-diffusivity heat flux model may look inconsistent with the full second-moment closure for the turbulent stress, as shown below, the results for the Nusselt number distribution on the impingement plane are in very good agreement with experiments.

Fig. 10 shows the Nusselt number $\left(Nu = \frac{q''_w D}{\lambda(T_w - T_{ref})}\right)$ distribution over the target wall computed with the three models: the $k-\varepsilon$ with wall functions, the $k-\overline{v^2}-f$ and EBM+GGDH models. For comparison, experimental results of Geers [2] obtained with liquid crystals are also shown.

As expected, the maximum heat transfer recorded experimentally and computed with all three models is achieved in the impingement regions, with *Nu* number showing a maximum at the stagnation points. However, despite the fact that the nozzles are circular, producing

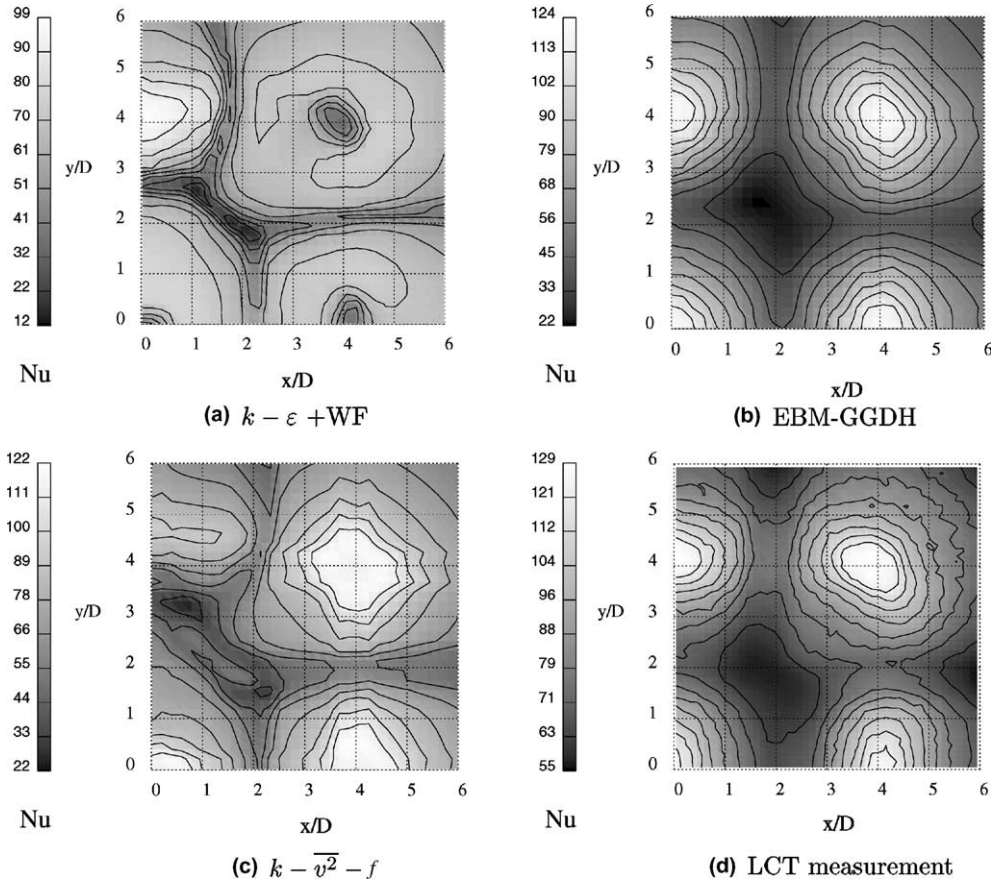

Fig. 10. Nusselt number distribution on the impingement plate.

initially round jets, the *Nu* number contours on the target plate are not of circular shape, but are deformed as a consequence of the interaction between the jets. Apart from the qualitative trend, the computational results look very different for the three models. The k–ε + WF model produced very erroneous results, both in the shape of the Nusselt number contours and in *Nu* magnitude. This is the consequence of the earlier discussed overprediction of the shift of the side jet, which leads to a peak value of *Nu* number under the side jet instead of the central one, and at the edges of the jet. Furthermore, in contrast to single impinging jets, where the standard k–ε model grossly overpredicts heat transfer in the stagnation region, here it does opposite: the stagnation point of the central jet shows no peak of the Nusselt number. This outcome is linked to the use of wall functions which are totally inadequate for this complex 3D flow, where in no region one can find even close resemblance with the equilibrium near-wall conditions on which the wall functions are based. The k–$\overline{v^2}$–f and EBM models, both with integration up to the wall, showed much improved shapes of the *Nu* contours and also the Nu magnitude. However, EBM performs significantly better and provides overall distribution of the *Nu* number in excellent agreement with experiments.

A further quantitative insight into the model performances can be gained from Fig. 11 showing profiles of the Nusselt number on the impingement plate along two lines, placed at $x/D = 0.0$ and $x/D = 4.0$. The failure of the standard k–ε model is very disturbing because at some locations, especially in the stagnation region of the central jet, but also of the side jet at $x/D = 4.0$, the behaviour is opposite from experiments and the values of the *Nu* number differ by factor of 3!

The k–$\overline{v^2}$–f model reproduces the general trend, congruent with the prediction of the velocity field. The peak *Nu* in the side jet is shifted outwards corresponding to the deformation of the velocity field discussed above (Fig. 4) and with a local peak at $y/D \approx 3.7$ in the cross-section $x/D = 0.0$, which coincides with the core of the embedded vortex shown in Fig. 9.

The EBM model shows best results. In view of the flow complexity, unavoidable uncertainties in experiments, and especially the performance of other models, the agreement with experiments can be regarded as remarkable, although at some location the difference in *Nu* numbers reaches 40%. It should be born in mind that the heat transfer model used here is relatively simple and it probably does not utilize the full advantage of having at disposal accurate EBM results for the velocity and stress field. The use of a more advanced heat flux model, such as Eq. (16) is expected to provide further improvements, but due to lack of time, this test remains still to be conducted.

It is noted that the model coefficient C'_θ is the only adjustable parameter in the GGDH heat flux model and that the value of 0.3, evaluated on the basis of wall equilibrium conditions (which only make sure that the same model will reproduce heat transfer in an equilibrium channel or boundary layer flow along a heated or cooled wall) proved to be a good choice. Computations with a slightly lower value, $C'_\theta = 0.25$ yielded the same curve only shifted slightly towards lower Nu.

For illustration we also show the computations obtained with the conventional isotropic eddy-diffusivity model ("simple-gradient diffusion hypothesis", SGDH) for the heat flux, $\overline{\theta u_i} = -\nu_t/\sigma_T \partial T/\partial x_i$. Despite realistic velocity and stress field (including kinetic energy k and, presumably, the dissipation rate ε, which should

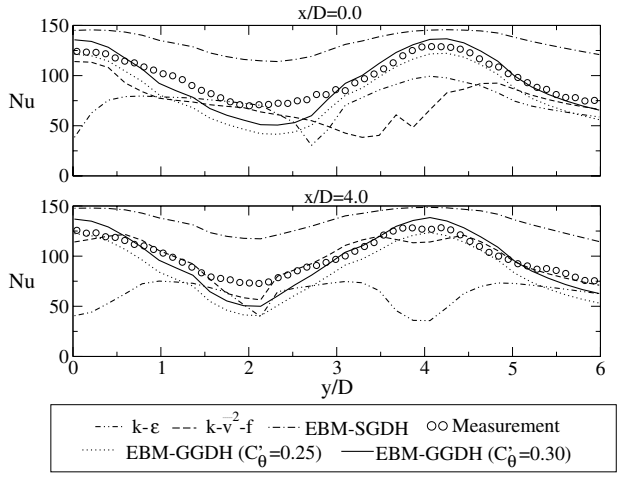

Fig. 11. Nusselt number on the target plane along two cross-sections, at $x/D = 0.0$ and 4.0.

provide accurate v_t), the distribution of the *Nu* number is wrong.

5. Concluding remarks

Turbulent flow and heat transfer in multiple-impinging jets have been studied computationally using an innovative second-moment turbulence closure with an elliptic blending model of the inviscid wall blocking effect, (EBM). The heat flux is at present modelled with a conventional anisotropic eddy-diffusivity model. The results are compared with experimental data, as well as with two eddy-viscosity/diffusivity models, the standard k–ε model with wall functions and Durbin's [10] k–$\overline{v^2}$–f elliptic relaxation model. A detailed comparison of the prediction of the flow and heat transfer in a square jets set-up confirmed the expectation that the flow is very challenging and difficult to reproduce with the eddy-viscosity models. The complex jet interaction, an outward shift of the side jet, the formation and collision of the wall jets on the impingement plate and the consequent upwash and recirculation in the space between the jets, were all reproduced successfully only with the EBM. Especially the $k-\varepsilon$ + WF gave very erroneous results, primarily because of inadequacy of the wall function approach in complex three-dimensional configurations. The k–$\overline{v^2}$–f model performed somewhat better, partly because of the integration up to the wall and partly because the elliptic relaxation equation in this model accounts reasonably well for the wall blockage, though not fully for the three-dimensionality of the turbulent stress field and its anisotropy.

The success in predicting the velocity and turbulent stress field is strongly reflected in the heat transfer predictions, confirming the importance of accurate capturing of the hydrodynamic field as a prerequisite for predicting the thermal field and heat transfer. Again the k–ε + WF returned erroneous Nusselt number distribution. The k–$\overline{v^2}$–f and EBM are much closer to the measured distributions, though the latter model proved to be visibly superior, providing very good agreement with the measurements.

Possible extensions of the EBM approach to provide an elliptic blending closure for the turbulent heat flux at the second moment level have been discussed, together with options for its truncation to an algebraic form. Whilst this route seems worth of future exploration, it has been shown that a conventional anisotropic eddy-diffusivity model suffices to reproduce Nusselt number, provided the accurate velocity and stress fields are at disposal. It is conjectured here that a combination of the EBM second-moment closure for the turbulent stress and the anisotropic (GGDH) eddy-diffusivity heat flux model can be used for reliable predictions of flow and heat transfer in complex configurations of industrial relevance. The price for using EBM in terms of increased computing time, which is about 50% higher than with the k–$\overline{v^2}$–f model using the same grid, seems justified in better prediction quality.

Acknowledgments

This research project was sponsored by The Technology Foundation (STW), TNO-TPD and Rademaker-Den Boer BV. The use of supercomputer facilities was sponsored by the National Computing Facilities Foundation (NCF) with financial support of NWO.

References

[1] L. Geers, M. Tummers, K. Hanjalić, Experimental investigation of impinging jet arrays, Exp. Fluids 36 (2004) 946–958.
[2] L. Geers, Multiple impinging jets: an experimental study of flow and heat transfer, Ph.D. Thesis, Delft University of Technology, 2004.
[3] M. Behnia, S. Parneix, P. Durbin, Prediction of heat transfer in an axisymmetric turbulent jet impinging on a flat plate, Int. J. Heat Mass Transfer 41 (1998) 1845–1855.
[4] M. Behnia, S. Parneix, Y. Shabany, P. Durbin, Numerical study of turbulent heat transfer in confined and unconfined impinging jets, Int. J. Heat Fluid Flow 20 (1) (1999) 1–9.
[5] T. Craft, L. Graham, B. Launder, Impinging jet studies for turbulence model assessment—II. An examination of the performance of four turbulence models, Int. J. Heat Mass Transfer 36 (10) (1993) 2685–2697.
[6] M. Dianat, M. Fairweather, W. Jones, Predictions of axisymmetric and two-dimensional impinging turbulent jets, Int. J. Heat Fluid Flow 17 (6) (1996) 530–538.
[7] T. Craft, Prediction of heat transfer in turbulent stagnation flow with a new second-moment closure, in: Proceedings of the Second EF Conference on Turbulent Heat Transfer, vol. 1, 1998.
[8] L. Thielen, H. Jonker, K. Hanjalić, Symmetry breaking of flow and heat transfer in multiple impinging jets, Int. J. Heat Fluid Flow 24 (4) (2003) 444–453.
[9] L. Thielen, Modelling and calculation of flow and heat transfer in multiple impinging jets, Ph.D. Thesis, Delft University of Technology, 2003.
[10] P. Durbin, Near-wall turbulence closure modeling without damping functions, Theoretical and Computational Fluid Dynamics 3 (1991) 1–13.
[11] G. Gerolymos, I. Vallet, Computation of 3-D aerospace configurations using a wall-normal-free Reynolds-stress model, in: Proceedings of the 5th International Symposium Engineering Turbulence Modelling and measurements, 2002, pp. 371–382.
[12] B. Basara, Employment of the second-moment turbulence closure on arbitrary structured grids, Int. J. Num. Methods Fluids 44 (4) (2004) 377–407.
[13] P. Durbin, A Reynolds stress model for near-wall turbulence, J. Fluid Mech. 249 (1993) 465–498.

[14] M. Gibson, B. Launder, Ground effects on pressure fluctuations in the atmospheric boundary layer, J. Fluid Mech. 86 (1978) 491–511.
[15] C. Speziale, S. Sarkar, T. Gatski, Modelling the pressure-strain correlation of turbulence: an invariant dynamical systems approach, J. Fluid Mech. 227 (1991) 245–272.
[16] R. Manceau, K. Hanjalić, Elliptic Blending Model: a new near-wall Reynolds-stress turbulence closure, Phys. Fluids 14 (2) (2002).
[17] S. Kenjereš, S. Gunarjo, K. Hanjalić, Contribution to elliptic relaxation modelling of turbulent natural and mixed convection, in: CD Proceedings Advanced Computational Heat Transfer III, Ankara, 2004.